PAPER • OPEN ACCESS

Mechanical response of an high-strength automotive steel at different strain rates and evolution of damage-related parameters

View the article online for updates and enhancements.

Mechanical response of an high-strength automotive steel at different strain rates and evolution of damage-related parameters

G Mirone[1*], R Barbagallo[1], M M Tedesco[2], D De Caro[2] and M Ferrea[2]

[1]Università di Catania, Dipartimento di Ingegneria Civile e Architettura, Via Santa
Sofia 64 – 95125 – Catania
[2]C.R.F. S.C.p.A, GML, Metals, Corso Settembrini 40, Torino

*gmirone@dii.unict.it

Abstract. The present work concerns a thin sheet high-strength steel of interest for automotive
applications. The extended constitutive curves in static and dynamic conditions were determined
by tensile tests on smooth specimens. Further tests carried out on notched specimens were
simulated both to validate the elastoplastic response and to analyse the evolution of the relevant
parameters related to ductile damage (triaxiality and Lode angle) in the critical areas of the
specimens (diffuse and localized necking), studying the correlations between the trend of these
quantities and the mode/location of the fracture initiation. The analysis of the images of the
specimens acquired during the tests allowed to characterize in detail the behaviour of the material
up to breakage, also providing different experimental references to validate the numerical
simulations of the tests on the smooth and notched specimens.

1. Introduction

The elastoplastic characterization of ductile materials, capable of large deformations, poses significant
problems because the onset of necking causes the loss of uniformity and uniaxiality of stress and strain
in the specimen. Therefore, afterwards, the equivalent stress-strain constitutive curve of the material can
no longer be obtained from the load and elongation histories of a tensile test.

In such cases the effective or *section-based* true curves should be firstly obtained, based on the
evolving load-minimum cross section ratio, and then a transformation should be applied to the former
true curves for converting them into estimates of the equivalent stress-strain curves.

The above estimate can be either derived from corrective formulas available in literature or from
inverse methods based on iterative finite element simulations.

The evolving resistant area of the specimen, necessary for deriving the area-based true curve, can
only be obtained with experimental techniques of increasing difficulty depending on the geometry of
the sample.

The minimum cross-section of cylindrical specimens and the related true strain beyond necking onset
can be monitored by diameter measurements through video recording and image analysis, quite simpler
and cheaper than usual DIC techniques [1] [2].

The true strain distribution over the neck of thin sheet specimens can be measured by 2D DIC
techniques, reliable until the onset of localized necking.

With thick rectangular specimens the derivation of the effective true curve is more difficult as the two previous techniques are not suitable. In such case only the 3D DIC can be used to reconstruct the entire specimen shape [3] [4][5].

Recently Mirone et al. [6] proposed a procedure, called MVB, capable of converting the current postnecking elongation into the current necked section of the specimen.

When the effective area-based true curve is not measured and its postnecking correction cannot be implemented, the adoption of inverse methods is mandatory, as in the work of Zhao et al. [7] where a method is presented to obtain the equivalent curve up to high deformation values through the correlation of simple tensile test and finite element analysis.

The specimens available for this work were not suitable to implement the MVB procedure and the successive postnecking correction, therefore a reverse approach has been used for the elastoplastic characterization of the steel.

Then the evaluation of the ductile damage of materials is also addressed here. The first stress invariant and the Lode parameter are known to govern ductile damage and failure of metals.

Among the most known phenomenological damage models, Bao and Wierzbicki [8] have proposed a damage model in which, for triaxiality levels higher than 1/3, the local breaking stress is expressed by a hyperbolic function of triaxiality averaged on the history of local deformation. Wierzbicki et al. [9] and Xue [10] have also implemented damage dependence on the Lode angle, which has long been known to affect the fracture of rocks and granular materials. Lode angle and stress triaxiality are also known to affect the yield surfaces of some metals, as pointed out in [11][12]. Brunig et al. [13] have derived a constitutive model for elastoplastic damage of materials using thermodynamics; in this case the variables that govern the evolution of the damage are plastic deformation, triaxiality and the Lode angle. Mirone & Corallo [14] implemented four failure models, where the Bao–Wierzbicki response to triaxiality is coupled to different Lode angle sensitivities. Mirone [13] also highlighted how the rise of stress triaxiality induced by the necking directly affects damage evolution and failure.

In the present work, a high-strength steel of interest in the automotive field, identified as TBC1180, is characterised at static and dynamic rates. Flat smooth specimens of different sizes and flat notched specimens with different geometries are cut from a metal sheet 1.56 mm thick, for being tested and simulated at different strain rates.

The elastoplastic characterization of the material at static and dynamic rates is carried out by reverse engineering based on finite element (f.e.) simulations of smooth specimens tests.

The constitutive curves thus obtained from flat smooth specimens are then validated by numerical-experimental comparisons of data related to the flat notched specimens. The matching of f.e. results against experimental data is made in terms of specimen force, elongation and lateral contraction histories during each test, which are also experimentally measured during the tests through video recording and successive image analysis.

The evolutions of the stress triaxiality and the Lode parameter are then obtained from the f.e. results at the critical nodes of the specimens, allowing the successive implementation of some models of ductile damage available in the literature.

2. Experimental campaign

For the characterization of the elastoplastic response of the high-strength steel TBC1180 at hand, four main sets of specimens have been considered with the geometries shown in Figure 1a.
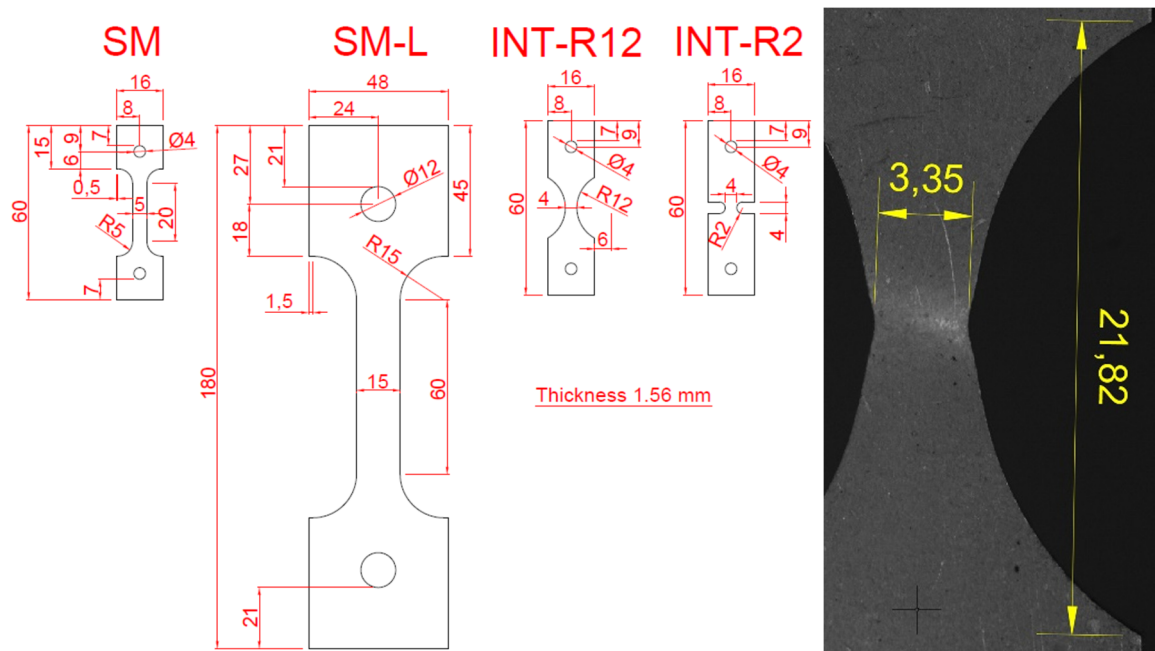
Figure 1. (a) Specimens geometries, (b) Example of a R12 specimen image

The tensile tests were performed at two different nominal deformation speeds. The static ones (3×10^{-3} s^{-1}) have been performed with a motor-driven machine and the dynamic ones (7 s^{-1}) with a hydraulic test machine. Furthermore, only the smooth specimens have also been tested at high temperature (150 °C and 300 °C) in static conditions and at high strain rate (350 s^{-1}) at room temperature with a Hopkinson bar apparatus. Table 1 summarizes the tests carried out.

The video recording of all static and dynamic tests, at room temperature and high temperature, have been acquired. Once scaled from a known size, the acquired images allow to follow the evolution of distances between experimental references, useful for the characterization and validation of constitutive curves, damage models and f.e. analysis (Figure 1b).

The geometric measurements acquired on each specimen are the elongation of a reference length (a gage length of about 15 mm and 50 mm in the small and large smooth specimens respectively, and the distance between the vertices of the notch in the notched specimens) and width of the minimum cross-section. These measurements are then associated with the tensile force value recorded by the load cell of the test machine at the same instants.

The elongations of the smooth specimens are used, together with the corresponding load values, to construct by points the nominal elongation based true curves, according to the known formulas shown in equations (1) and (2).

$$\varepsilon_{L-True} = Ln\left(\frac{L}{L_0}\right) \tag{1}$$

$$\sigma_{L-True} = \frac{F}{A_0}\left(\frac{L}{L_0}\right) \tag{2}$$

The width reduction of the smooth specimens is instead related to both the load, for FEM/Experimental validation, and to the elongation, useful for calculating the necking strain as better specified below.

Table 1. Experimental campaign

Specimen type	Test Name	Reference True Strain Rate [s⁻¹]	Gage length [mm]	Test Environment Temperature [°C]
SM	S-T22-01	0.0006	14.85	22
	S-T30-01	0.0006	17.82	30
	S-T30-02	0.0006	15.31	30
	D7-01	7.5	15.31	20
	D7-02	7.5	14.92	20
SML	S-T30-01	0.0006	52.51	30
	S-T30-02	0.0006	53.58	30
INT-R2	S-01	Machine speed = SM-S	4	15
	S-02	Machine speed = SM-S	4	15
	D7-01	Machine speed = SM-D7	4	20
	D7-02	Machine speed = SM-D7	4	20
INT-R12	S-01	Machine speed = SM-S	20.7	15
	S-02	Machine speed = SM-S	20.7	15
	D7-01	Machine speed = SM-D7	20.7	20
	D7-02	Machine speed = SM-D7	20.7	20

3. Static tests at room temperature

The results of the static tests at room temperature carried on the small (SM) and large (SML) smooth specimens are shown in Figure 2 and Figure 3 in terms of nominal elongation-based true curves and force-width variation curves. The SM-S-T22-01 test has been carried on in two parts because of missing camera recording in the first phase, therefore only the second part is shown, with an initial strain of about 0.04.

In all the smooth large samples it was possible to evaluate very similar gage lengths, therefore the corresponding nominal elongation-based true curves are comparable up to fracture. On the other hand, slightly different gage length have been considered for the small smooth specimens, therefore the corresponding curves are comparable only before necking, slightly diverging afterwards.

The nominal true curves obtained from small and large smooth specimens are very similar before necking, demonstrating that the geometric differences do not cause differences in the constitutive curves. After necking, the nominal length-based true curves lose their validity and, therefore, it is not possible to make a comparison between the two tests series on small and large samples.

The nominal true curves obtained from small and large smooth specimens are very similar before necking, demonstrating that the geometric differences do not cause differences in the constitutive curves. After necking, the nominal length-based true curves lose their validity and, therefore, it is not possible to make a comparison between the two tests series on small and large samples.

The constitutive curve coincides with the nominal true curve until necking and then diverges: it is, therefore, necessary to identify the necking strain to know how far the experimental curve correctly expresses the flow curve, and then identify the post-necking constitutive curve through an inverse iterative approach. In order to precisely identify the necking strain, in addition to the evaluation of maximum force instant, the volume conservation of a prismatic part of the specimen has been considered. The necking instant is the one in which the considered volume loses its prismatic shape.
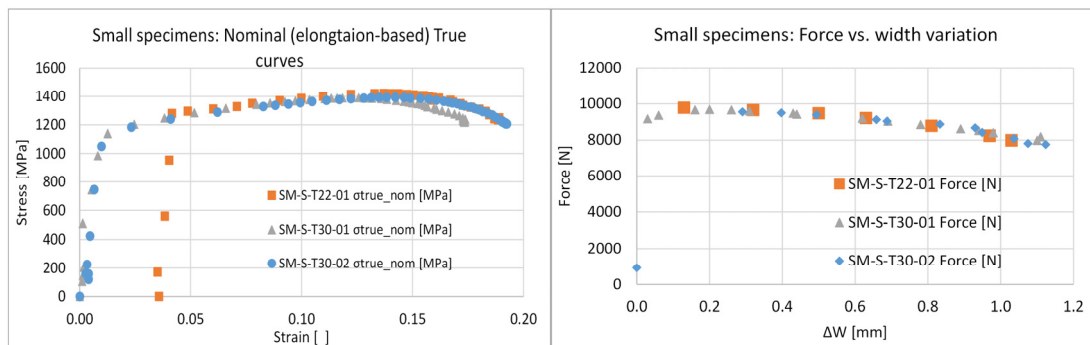
Figure 2. Static tests at room temperature on small smooth specimens: nominal elongation-based true curves (a) and load-width variation curves (b).
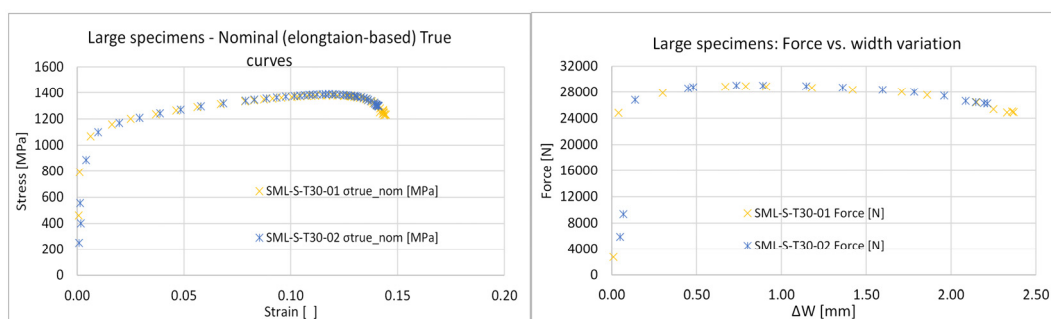

Figure 3. Static tests at room temperature on large smooth specimens: nominal elongation-based true curves (a) and load-width variation curves (b).

The obtained necking strain in static conditions at room temperature is 0.11. The obtained constitutive curve is shown in Figure 4a, together with the experimental nominal true curves from small smooth specimens. In the same figure, the fracture point is highlighted with a star; the corresponding shape at fracture of the f.e. model is shown in Figure 4b.
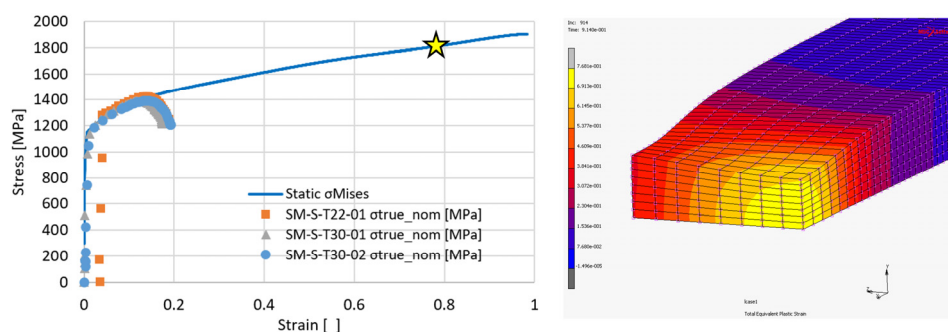

Figure 4. Static tests at room temperature: (a) constitutive Mises curve compared to the experimental nominal true curves from small smooth specimens and (b) f.e. model shape at fracture.

The static constitutive curve of Figure 4a, implemented in a f.e. code, provides a good agreement with respect to the experimental load-elongation and load-width curves, for both smooth specimens, used for reverse calibration of the constitutive curve, and notched specimens, whose numerical/experimental comparison is introduced only during the validation phase of the constitutive curve, as shown in Figure 5.
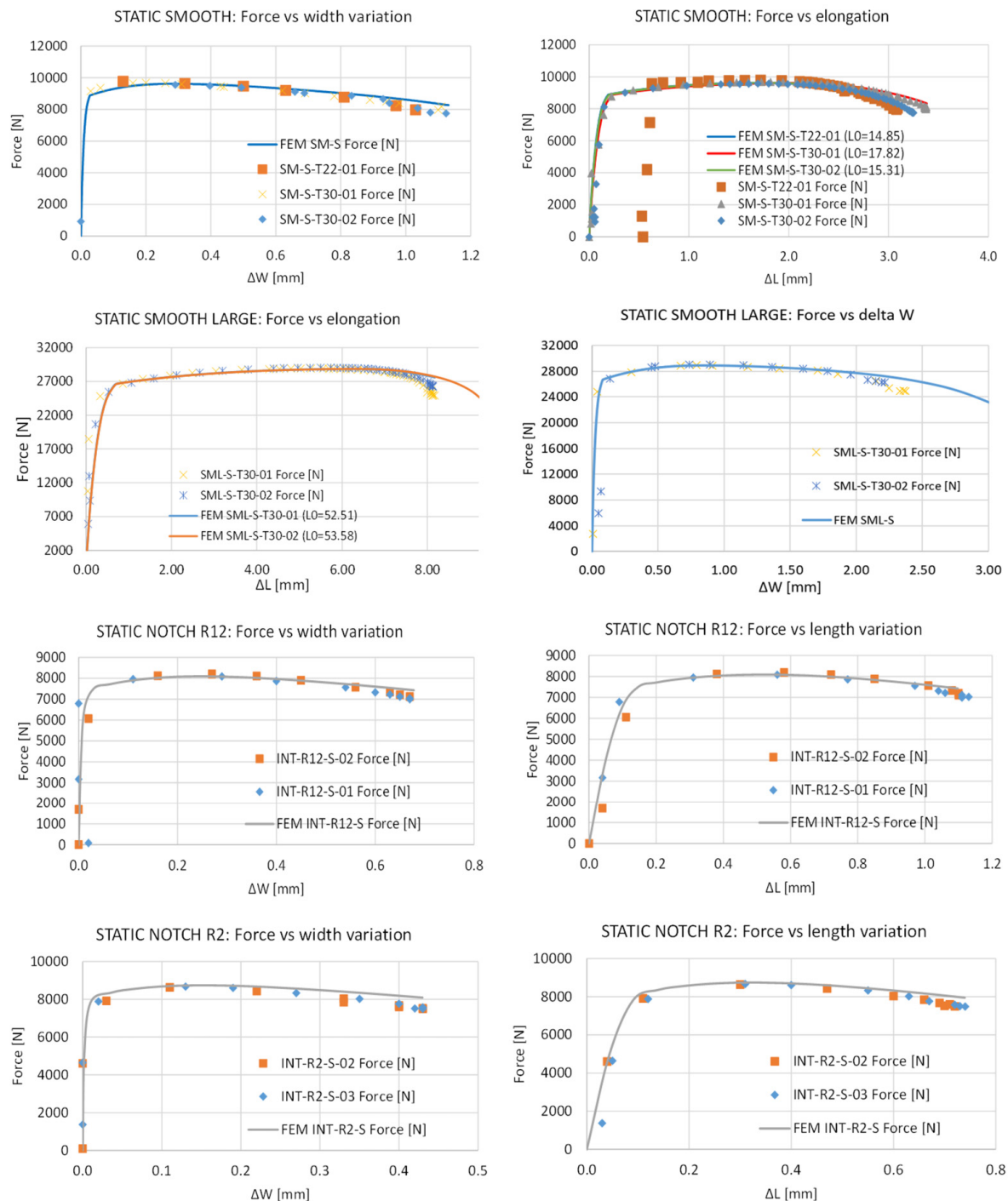
Figure 5. Experimental/numerical comparison for all the static tests at room temperature on smooth and notched specimens.

4. Dynamic tests at intermediate strain rate (7 s⁻¹) at room temperature

Following the same procedure, the necking strain and the constitutive curve at intermediate strain rate (7 s-1) at room temperature have been evaluated. The first is 0.13 while the latter is shown in Figure 6a compared to the experimental nominal true curves. In Figure 6b are shown the nominal true strain rate vs nominal true strain experimental histories.
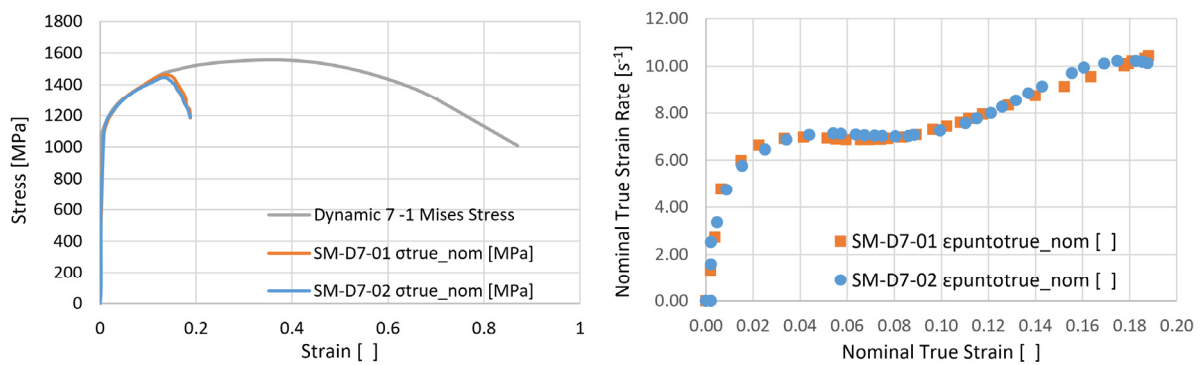
Figure 6. Dynamic tests at room temperature at 7 s^{-1}: (a) constitutive curve compared to the experimental nominal true curves and (b) nominal true strain rate vs nominal true strain experimental histories.
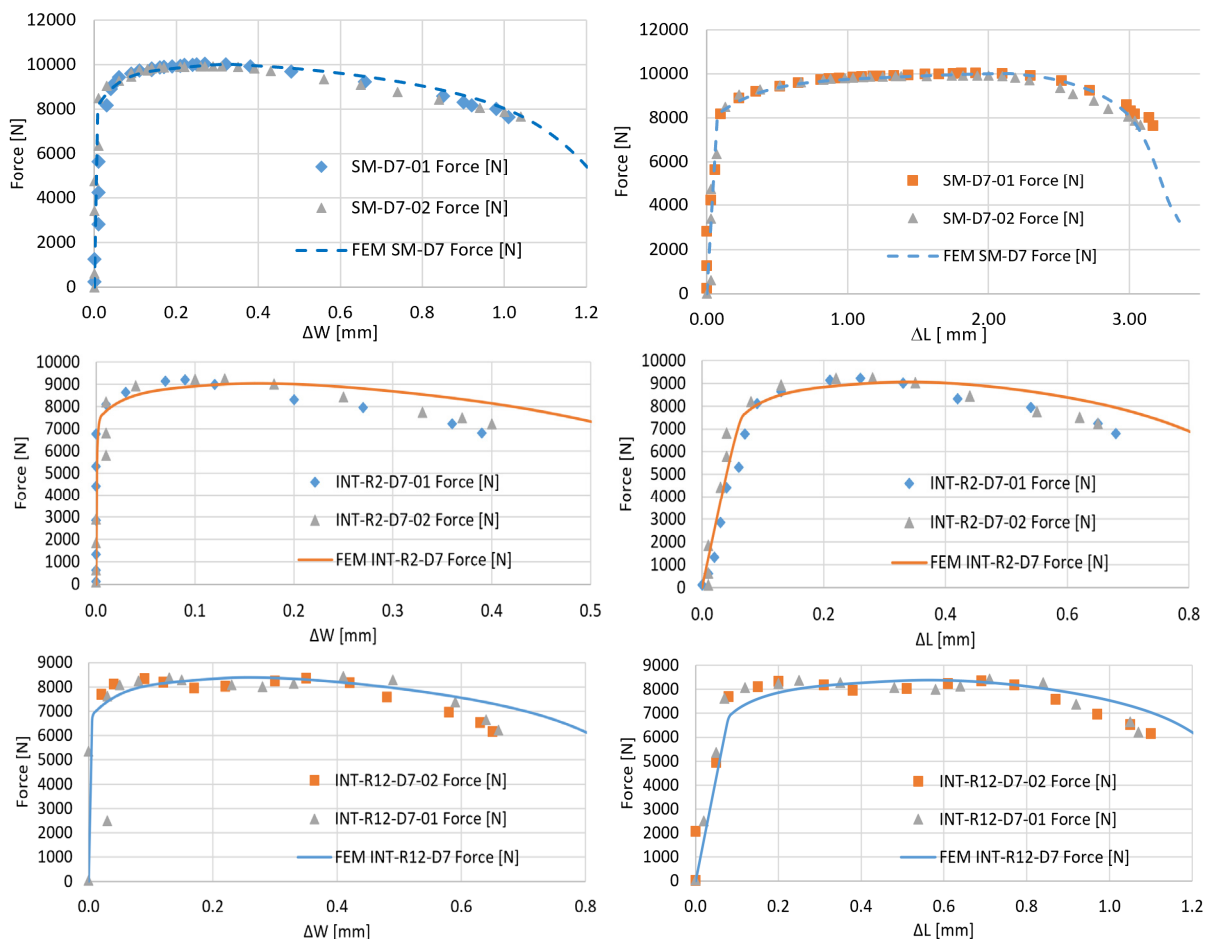

Figure 7. Experimental/numerical comparison for all the dynamic tests (7 s^{-1}) at room temperature on smooth and notched specimens.

As shown in Figure 7, the dynamic 7 s^{-1} constitutive curve of Figure 6a, implemented in a f.e. code, provides a good agreement with respect to the experimental load-elongation and load-width curves for smooth specimens, used for reverse calibration of the constitutive curve. The numerical-experimental comparisons relating to the notched specimens show a good agreement until just before the break, where the simulated curves slightly overestimate the load or the width/elongation.

It is useful to emphasize that the dynamic constitutive curve includes the effects of dynamic amplification due to strain rate and thermal softening triggered by the inability to transmit the plastic work converted into heat into the environment. The comparison between the static and the dynamic curves is shown in Figure 8. Up to about 0.3 of equivalent plastic deformation, there is a modest prevalence of dynamic amplification over thermal softening (dynamic curve higher than static one), while over 0.3 the temperature of the specimen has risen enough to quickly prevail thermal softening over the dynamic amplification (dynamic curve drops below the static).
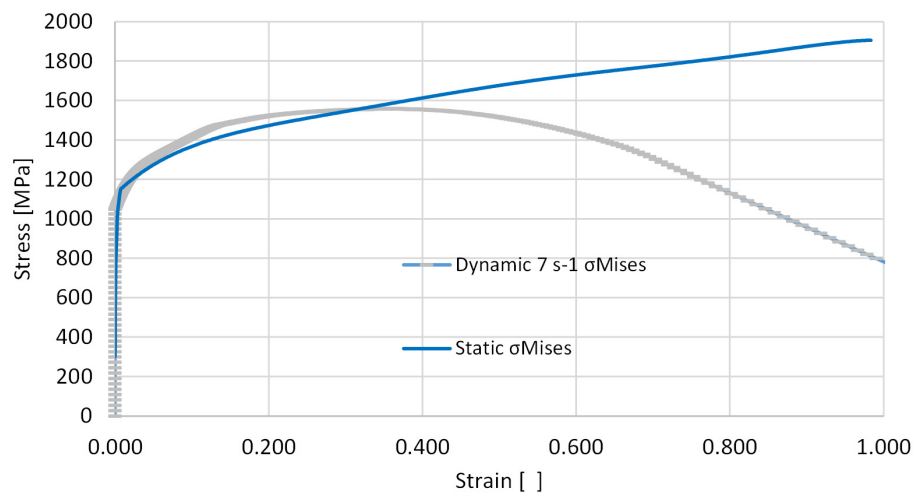

Figure 8. Static and dynamic 7 s^{-1} constitutive curves comparison.

5. Ductile damage modelling

From the f.e. analysis validated with macroscopic references, it is possible to extract the trends of significant quantities related to ductile damage, as triaxiality factor TF and normalized Lode angle X, on the significant nodes of the specimen. With these trends, it is possible to implement several decoupled damage models a posteriori, i.e. damage models that depend indirectly on the hardening laws (and deformation histories), but which in turn do not affect the hardening itself.

The trends of these quantities, coming from the f.e. simulations, were extracted for all simulated tests on the critical node, always found to be the central one of the neck section, both for static and dynamic tests. Figure 9 shows these TF and X trends as the equivalent plastic strain varies. On each curve, three points are highlighted corresponding to the experimental rupture conditions identified by the load (circle), the elongation (square) and the friction (triangle). Here we proceed using the load breaking condition, except in some cases where the achievement of this condition on the load is unrealistic: for example, for the simulation of the dynamic test on smooth specimen, the achievement of the breaking load would require excessively large elongations and width variations compared to the experimental ones.
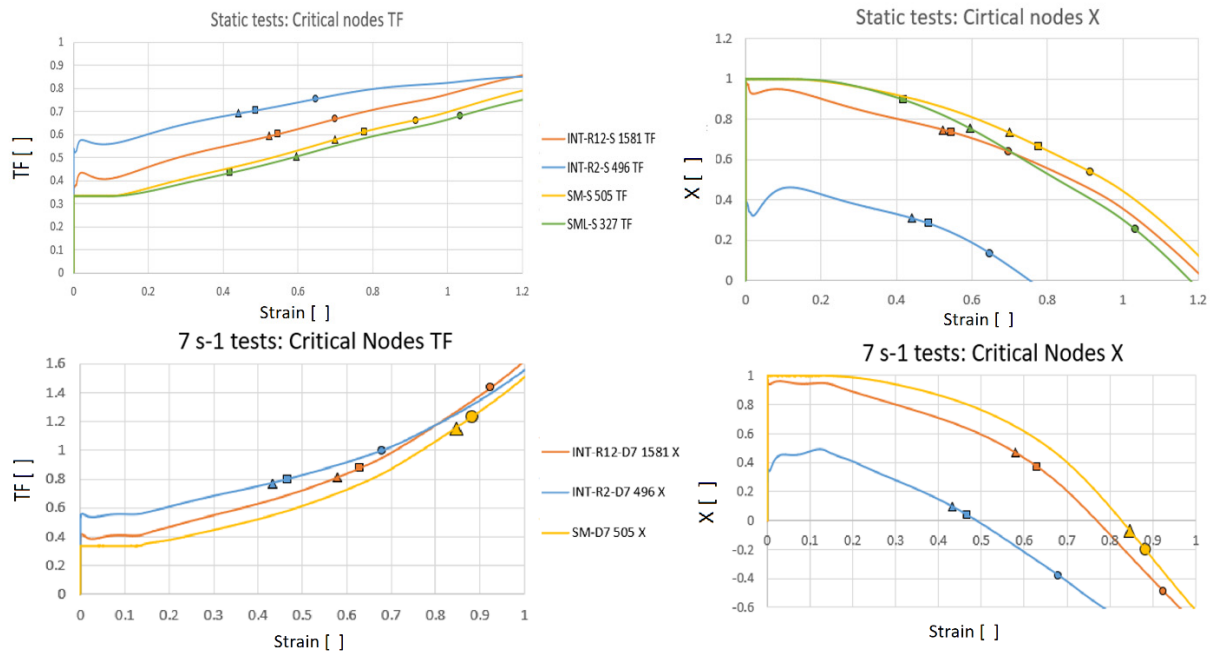
Figure 9. TF and X versus plastic strain at the neck centre for in static and dynamic tests

As shown in Figure 9, the theoretical values of triaxiality and Lode angle, relating to the initial geometry of the specimen, undergo very significant changes due to the large deformations that occur locally: the triaxiality at the center of the neck of a smooth specimen, which theoretically is around 0.33, actually at incipient breakage doubles (static tests) or triples (dynamic tests). Similarly, the normalized Lode angle, which theoretically holds 1 for a uniaxial state such as that of the smooth pre-necking specimen, at break due to the necking becomes even negative for the dynamic tests simulated with the curve of Figure 8.

The damage models considered here are that of Bao-Wierzbicki (BW) [8], and the model proposed by Mirone and Corallo [14] identified as D4.

5.1. Bao-Wierzbicki damage model

The BW model considers that the damage depends only on the plastic strain - triaxiality combination and is proposed as equation (3), where ε_{Cr-BW} is the critic strain at which the material point fails, D_{CR} is the critic damage, material constant to be calibrated and TF_{Avg} is the averaged TF, obtained as in equation (4).

$$\varepsilon_{Cr-BW} = \frac{D_{CR}}{TF_{Avg}} \tag{3}$$

$$TF_{Avg} = \frac{1}{\varepsilon_{Cr-BW}} \cdot \int_0^{\varepsilon_{Cr-BW}} TF \, d \, \varepsilon_{Eq} \tag{4}$$

If it is not the case of proportional loading, as in all the experiments considered here, TF varies greatly during each test and such criteria must be used in the form shown in equation (5), in which D_{BW} is the damage which evolves from zero to the critical value D_{CR}, and the unknown variable is the critic strain ε_{Cr-BW}.

$$D_{BW} = \int_0^{\varepsilon_{Cr-BW}} TF \, d \, \varepsilon_{Eq} \leq D_{CR} \tag{5}$$

Figure 10 shows the BW damage curves extended up to the breakage for each test. In this way it can be assessed whether/how much these curves allow for effectively constant critical damage values for the material in static and dynamic conditions, independent of the geometry of the specimen.
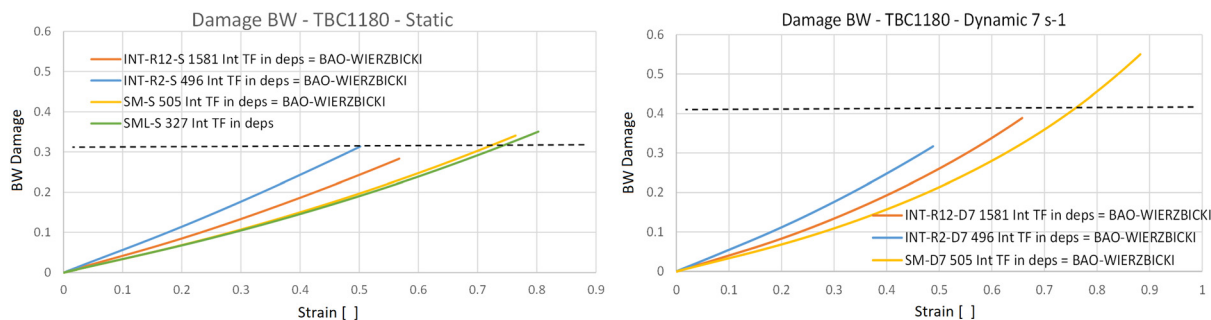

Figure 10. Static and dynamic tests: BW damage evolution versus strain

While in static conditions the steel at hand adapts rather well to the BW model with a $D_{CR} \approx 0.32$ and modest dispersion around this value, in dynamic conditions it is observed that the average value $D_{CR} \approx 0.42$ is not really representative of the damage to the three tests due to of the remarkable dispersion.

5.2. Mirone-Corallo D4 damage model

The next damage model considered is the D4 [14], which incorporates the same dependence on TF proposed by Bao and Wierzbicki, adding a dependence on X as in eq. (6), in which $C_0 + C_1 = 1$. Therefore, there are three material constants to be calibrated: C_0, C_2 (Lode angle effect) and D_{Cr} (triaxiality effect in case of tests with X=1).

$$D_4(\varepsilon_{Eq}) = \frac{\int_0^{\varepsilon_{Cr}} TF \cdot d\varepsilon_{Eq}}{C_0 + C_1 \cdot \left[1 - Cos\left(\frac{\pi}{2} \cdot X_{Avg}\right)\right]^{C_2}} \leq D_{Cr} \tag{6}$$

The calibration is made imposing that the denominator of the damage function, called here $g(X)$ and shown in equation (7), approximates the points representing the ratios between the integrals of TF and the D_{Cr}.

$$g(X_{Avg}) = C_0 + C_1 \cdot \left[1 - Cos\left(\frac{\pi}{2} \cdot X_{Avg}\right)\right]^{C_2} = \frac{\int_0^{\varepsilon_{Cr}} TF \cdot d\varepsilon_{Eq}}{D_{Cr}} \tag{7}$$

Figure 11 reports the function $g(X)$ corresponding to four different sets of parameters, plotted together with the discrete points used for its calibration in the case of the static tests. It is visible that the available calibration data can be approximated by different sets of calibration data because the points are close to each other around $X_{Avg} = 1$ while no data is available for $X_{Avg} < 0.4$. The availability of calibration points around $X_{Avg} < 0.2$ might solve the issue and lead toward a unique set of model parameters. Here, two arbitrary sets of model constants are selected among those matching the available static and dynamic data respectively.
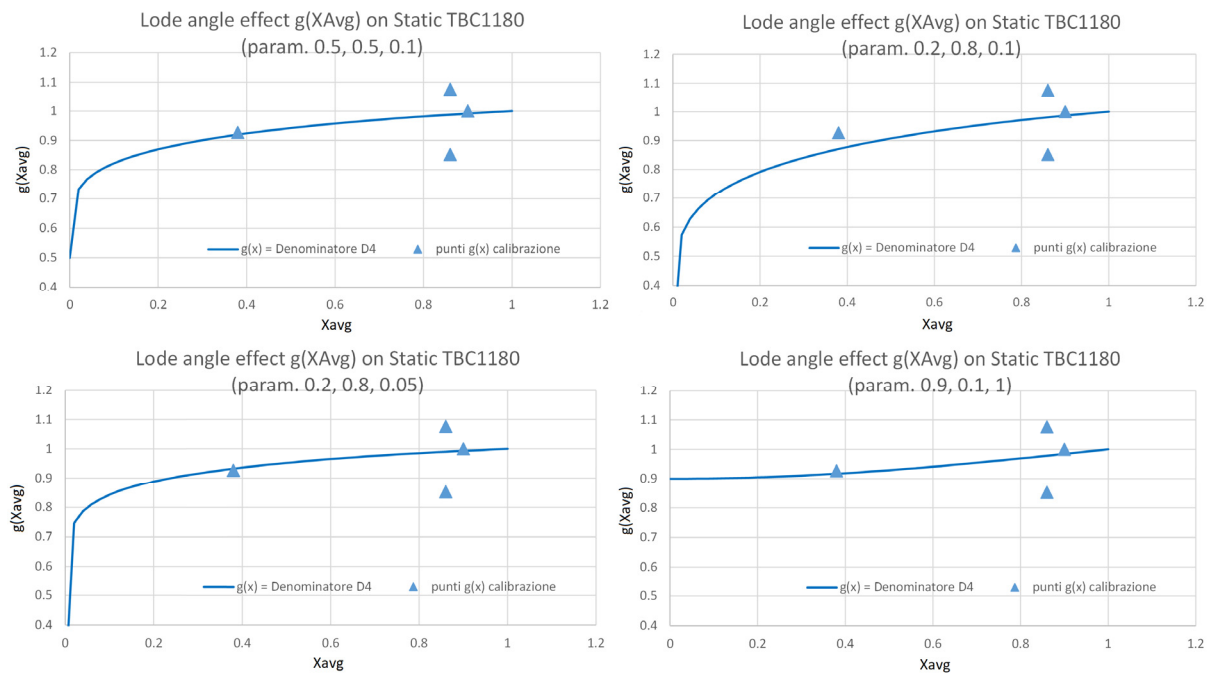
Figure 11. D4 damage: evolution of the g function with four different model constants sets for the static case.

Figure 12 shows, for both dynamic and static conditions, the function $D_4\left(\varepsilon_{Eq}\right)$ for static and dynamic tests, with constants sets reported in the title of each graph. For the static tests the D4 damage model provides a good accuracy, similar to that of the Bao-Wierzbicki model, while for dynamic tests it slightly improves the response of the model BW.
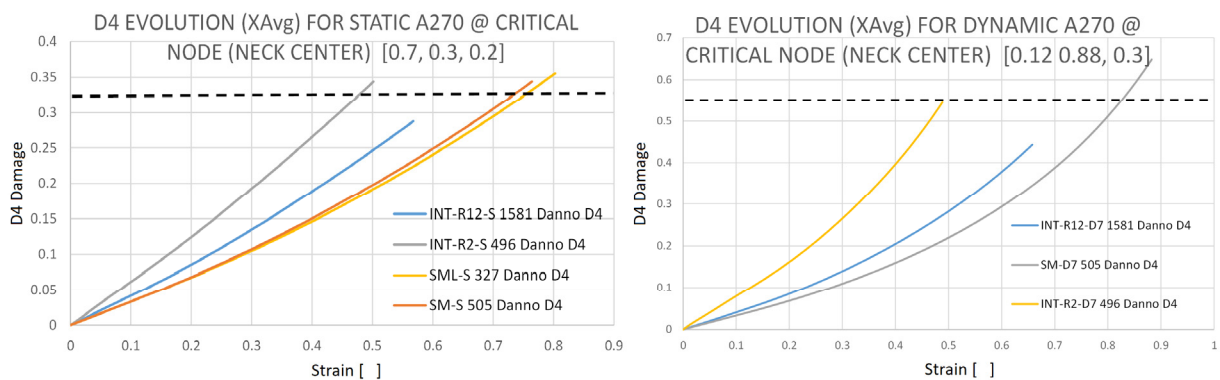

Figure 12. D4 damage evolution

6. Conclusions

Static and dynamic tests on TBC1180 steel flat specimens allowed to characterize the material at two different deformation speeds, allowing to simulate with reasonable accuracy the mechanical response (loading, elongation, width contraction) of smooth and notched specimens.

The numerical analyses, validated considering the above experimental references, allowed to determine the evolution of the relevant parameters related to ductile damage, i.e. triaxiality factor and Lode parameter, on critical nodes internal to the material where no real local measurement is possible.

This observation has shown that the large deformations typical of a ductile metal cause important variations of the triaxiality and deviatoric parameters with respect to the theoretical values of the undeformed specimen, thus not allowing the use of many damage models in the form of a failure criterion while imposing their use in the form of a damage function to be calculated during the deformation history, up to the achievement of critical values to be determined by calibration.

Furthermore, the use of flat specimens, even without notch, does not allow to obtain the constant unit value of the normalized Lode angle, which does not allow to accurately calculate the value of the critical damage, making the calibration of the Bao-Wierzbicki model and of the models derived from it less immediate.

The experimental data set available allowed a complete calibration of the BW damage model while a partial calibration of the D4 model, for which a free parameter remains. The BW model proves to be reasonably accurate for static tests while it is poorly suitable for predicting the failure of dynamic tests. The D4 model maintains the already acceptable accuracy of the BW model for static tests, while for dynamic tests it provides a slightly improved accuracy with respect to the BW model.

References

[1]   Mirone, G., Barbagallo, R., Corallo, D., & Di Bella, S. (2016). Static and dynamic response of titanium alloy produced by electron beam melting. Procedia Structural Integrity, 2, 2355-2366.

[2]   Mirone, G., Barbagallo, R., & Giudice, F. (2019). Locking of the strain rate effect in Hopkinson bar testing of a mild steel. International Journal of Impact Engineering, 130, 97-112.

[3]   Grytten, F., Daiyan, H., Polanco-Loria, M., & Dumoulin, S., (2009). Use of digital image correlation to measure large-strain tensile properties of ductile thermoplastics. Polymer Testing, 28(6), 653-660.

[4]   De Almeida, O., Lagattu, F., & Brillaud, J., (2008). Analysis by a 3D DIC technique of volumetric deformation gradients: Application to polypropylene/EPR/talc composites. Composites Part A: Applied Science and Manufacturing, 39(8), 1210-1217.

[5]   Ehlers, S., & Varsta, P., (2009). Strain and stress relation for non-linear finite element simulations. Thin-Walled Structures, 47(11), 1203-1217.

[6]   Mirone, G., Verleysen, P., & Barbagallo, R. (2019). Tensile testing of metals: Relationship between macroscopic engineering data and hardening variables at the semi-local scale. International Journal of Mechanical Sciences, 150, 154-167.

[7]   Zhao, K., Wang, L., Chang, Y., & Yan, J. (2016). Identification of post-necking stress–strain curve for sheet metals by inverse method. Mechanics of Materials, 92, 107-118.

[8]   Bao, Y., & Wierzbicki, T. (2004). On fracture locus in the equivalent strain and stress triaxiality space. International Journal of Mechanical Sciences, 46(1), 81-98.

[9]   Wierzbicki, T., Bao, Y., Lee, Y. W., & Bai, Y. (2005). Calibration and evaluation of seven fracture models. International Journal of Mechanical Sciences, 47(4-5), 719-743.

[10]   Xue, L. (2009). Stress based fracture envelope for damage plastic solids. Engineering Fracture Mechanics, 76(3), 419-438.

[11]   Bai Y. Wierzbicki T.,, A new model of metal plasticity and fracture with pressure and Lode dependence, International Journal of Plasticity, 24-6, 1071-1096.

[12]   Mirone, G., Barbagallo, R., Corallo, D., A new yield criteria including the effect of lode angle and stress triaxiality, Procedia Structural Integrity 2, pp. 3684-3696.

[13]   Brünig, M., Chyra, O., Albrecht, D., Driemeier, L., & Alves, M. (2008). A ductile damage criterion at various stress triaxialities. International journal of plasticity, 24(10), 1731-1755.

[14]   Mirone, G., Corallo D. (2013). Stress–strain and ductile fracture characterization of an X100 anisotropic steel: Experiments and modelling. Engineering Fracture Mechanics 102, (2013) 118–145.

[15]   Mirone, G., Approximate model of the necking behaviour and application to the void growth prediction, 2004, International Journal of Damage Mechanics 13-3, 241-261.